Investigation on supersonic, large wall roughness elements using QIRT and PIV

by N. A. Voogt*, B.W. van Oudheusden* and F.F.J. Schrijer*

*Delft University of Technology, Aerospace Engineering Department
Kluyverweg 1, 2629 HS, Delft, The Netherlands
nickvoogt@gmail.com, b.w.vanoudheusden@tudelft.nl, f.f.j.schrijer@tudelft.nl

Abstract

The aim of the present study is to quantify the influence of large, ribbed wall roughness elements on the mean flow and heat transfer properties of a turbulent, supersonic boundary layer (M = 2.0). Fifteen test geometries, including one smooth and fourteen rough surfaces are tested using Schlieren, PIV and QIRT. Heat transfer measurements were obtained by the heated-thin-foil method, providing a constant heat flux boundary condition. The QIRT setup was designed to yield an accurate mapping of the surface temperature. It was observed that the geometries followed supersonic, single-cavity type flow classifications with clear, distinguishable flow features.

1. Introduction

The topic of the present study is the characterisation of the flow field and surface heat transfer properties of supersonic flow over a surface equipped with discrete, large-scale, 2D, rib-type roughness elements. The turbulating and associated mixing-enhancing effects of such geometries are relevant to applications such as heat-exchanger elements, which have been notably investigated for subsonic conditions [1,2,3]. In contrast to the distributed effect of sandpaper-like roughness, the periodic roughness elements behave as discrete elements when the rib height exceeds approximately 20% of the boundary-layer thickness [4,5]. The resulting flow over the ribbed surface can then be regarded as a *repeated cavity* flow, where for increasing separation-to-rib-height-ratio, the flow pattern in between each rib pair changes from an open to transitional to closed cavity flow type.

Most investigations regarding the effects of large-scale ribbed roughness elements have been reported for subsonic flow conditions. The most important geometric variables for periodic square-rib roughness geometries are the pitch-to-height ratio (p/e) and the rib height relative to the boundary layer thickness (e/δ). These researches focussed mostly on heat transfer, but also flow properties were addressed, see for example Han (1984), Han et al. (1985), Liou and Hwang (1992) and Aliaga et al. (1993) [2,3,7,1]. The investigations showed an increase in both average skin friction and heat transfer when increasing the relative rib height, while these were found to decrease when increasing the p/e of the roughness geometries in the range $10 \leq p/e \leq 40$. In contrast to the investigations performed for subsonic flows, the data on the effect of surface geometry under supersonic conditions is relatively scarce. Latin and Bowersox (2000) measured the boundary layer properties resulting from several smaller roughness types ($e/\delta < 0.2$), including two-dimensional, square-ribbed roughness elements [6]. It was found that the mean flow and turbulence properties of the supersonic boundary layers are differently affected by two-dimensional, periodic roughness as the turbulence levels increase by up to 25% compared to equivalent, randomly-distributed, three-dimensional sand-grain roughness.

In view of the above, the aim of the present study is to obtain quantitative insights on the influence of large ($e/\delta \geq 0.2$), ribbed wall roughness elements on the heat transfer of a turbulent, supersonic boundary layer, in order to complement the existing data base on the heat transfer characteristics and associated flow topologies of these geometries. These experimental results are intended to reveal which flow phenomena have the most dominant effect on the heat transfer characteristics of each roughness configuration. In addition, it is desired to find whether from the range of wind tunnel models investigated, a roughness configuration can be identified that maximizes heat transfer.

2. Experimental set-up

The experiments consider turbulent, supersonic boundary layer flow over a variety of ribbed wall surfaces. The Mach number of the freestream is 2.0, while the undisturbed boundary layer height is approximately 6 *mm* [8]. A total of fifteen test geometries, including one smooth and fourteen rough surfaces, consisting of various relative roughness heights, e/δ, and pitches, p/e, were investigated. For the heat transfer measurements, quantitative infrared thermography (QIRT) is utilized. In addition, the flow field is investigated using Schlieren visualization while particle image velocimetry (PIV) is used to quantify the mean flow and turbulence properties.

2.1. Supersonic wind tunnel

The experiments were conducted in the ST-15 blow down wind tunnel, at the High Speed Laboratory (HSL) of the Aerospace faculty of the Technical University of Delft. The tunnel has a 0.16 x 0.15 m^2 test section and a fixed nozzle geometry (figure 1) which provides a freestream Mach number of 2.0. The total temperature in the settling chamber is

License: https://creativecommons.org/licenses/by/4.0/deed.en

equal to $T_0 = 290\ K$ and the total pressure is $P_0 = 3.2 \cdot 10^5\ N/m^2$. This results in a free stream velocity of $u_\infty = 509\ m/s$ and a corresponding unit Reynolds number of $Re_u = 3.7 \cdot 10^7\ m^{-1}$. In the experiments, the turbulent boundary that develops along the walls of the wind tunnel is used. In previous experiments it was established that the boundary layer thickness was $\delta_{99} = 6.0\ mm$ [8]. On either side of the test section glass windows can be installed (for Schlieren visualisation), in which case the roughness plates are integrated in the wind tunnel bottom wall. Alternatively, for the QIRT experiments, a Germanium window is installed on one side while the opposite window flange is used to mount the heated test plates (figure 2). This allows the IR camera optimal viewing angles with respect to the test plates.

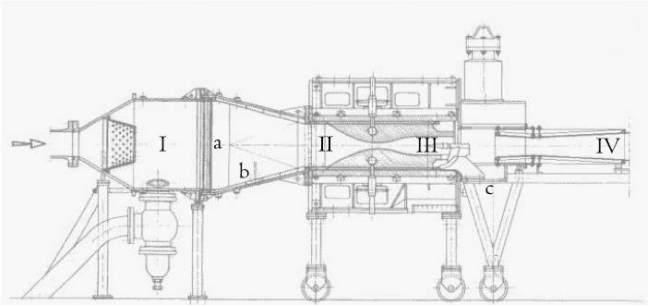

***Fig. 1**: Technical drawing of ST-15 wind tunnel.*

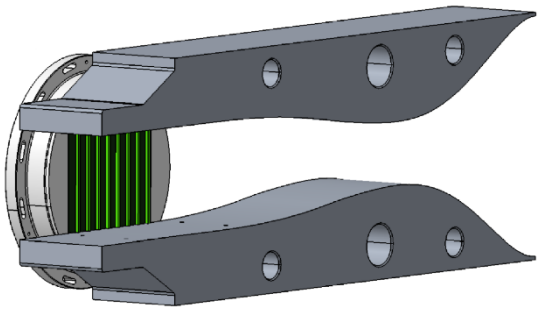

***Fig. 2**: CAD drawing of the QIRT model setup, excl. Germanium window normally mounted on the right.*

2.2. Wind tunnel models

The test plates, that are installed in a dummy window frame for the QIRT experiments have a length of 178 *mm* in the streamwise direction and a width of 150 *mm* such that they cover the complete height of the test section. As was already mentioned in the previous section, the opposite flange was used to install a Germanium window such that the IR camera has optimal viewing angles with respect to the test plates. A reference of the geometrical definitions of the wind tunnel models is displayed in figure 3, where p corresponds to the face-to-face distance between ribs, e indicates the rib height and x_0 is the fixed location of the first roughness element as seen from the leading edge of the insert.

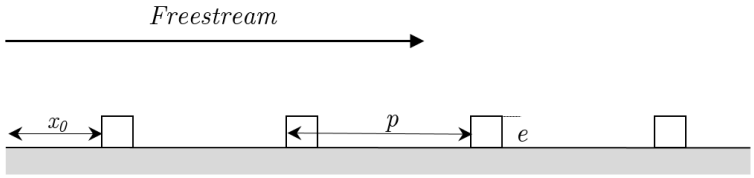

***Fig. 3**: Definition of the parameters governing the roughness geometry.*

2.3. Experimental setup

The heat transfer measurements are performed by means of the heated-thin-foil technique [11], where a custom designed printed circuit board (PCB) constitutes the 'thin foil'. A Cedip Titanium 530L Infrared camera is used to map the temperature distribution on the top surface of the model, whilst 16 K-type thermocouples are mounted on the sides and rear in order to obtain a complete thermal characterization of the models. The QIRT setup was designed such as to provide an approximately constant heat flux boundary condition on the exposed surface with known material characteristics. This then results in an accurate and reliable mapping of the temperatures across each surface of the interchangeable test models.

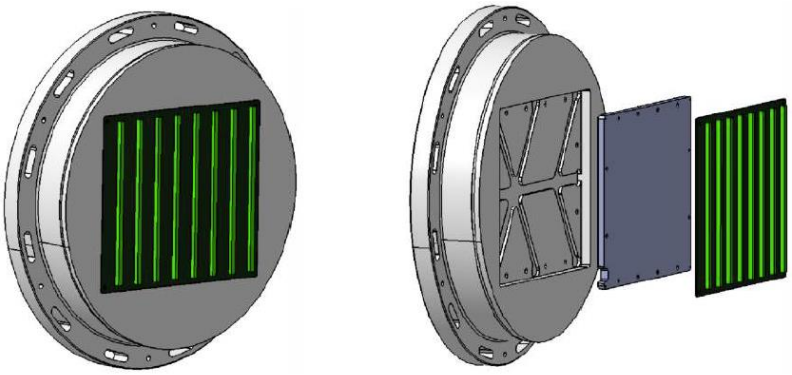

***Fig. 4**: Test plate within the cavity door, mounted (left) and exploded view (right), Makrolon insulation (grey), PCB substrate (black) and SikaBlock ribs (green).*

Each model consisted of an assembly of an 8 *mm* thick Makrolon insulation layer, the PCB surface and geometry-specific SikaBlock ribs (figure 4). The constant heat flux boundary condition was created by applying electric power to the PCB, delivering Ohmic heating. By tailoring the amount of electric power, steady-state conditions were reached within an average time of 23 *sec* at a temperature contrast of 37 *K*.

The test plate design and material characteristics (i.e. thermal diffusivity, α) are such that the conductive heat loss into the adjoining aluminum cavity door is minimal (i.e. $q_{cond} < 0.01 q_{el}$). Furthermore, steady-state conditions and sufficient thermal contrast can be reached with a relatively limited electric power input of approximately 500 *W*. Finally, this design enables the user to interchange the test plates relatively easily.

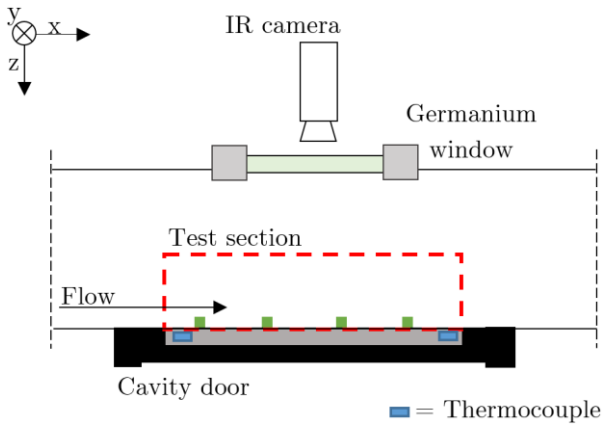

***Fig. 5**: Schematic of the experimental setup (upper view).*

A schematic of the experimental setup is shown in figure 5, where the IR camera observes the test plate through the Germanium window from the top. In order to mitigate interference from the ambient, the IR camera is shielded by a thick black cloth and anti-reflective screens. In order to measure the temperature of the rear and sides of the Makrolon insert, 16 K-type thermocouples were installed at specific locations. Furthermore, a J-type thermocouple is placed inside the settling chamber to determine the total temperature T_0 of the wind tunnel free stream. This temperature data is recorded through a multi-channel NI-9124 acquisition and TB-9214 isothermal terminal block at a frequency of 2 *Hz*. In high accuracy mode, the average thermocouple measurement accuracy is equal to 0.36 *K* whilst – at 25 *Hz* – the IR camera's NETD is equal to 25 *mK*.

3. Camera calibration

To accurately convert the camera output in digital levels (*DL)* into temperature (*K*), a calibration is performed at conditions which includes all (external) effects of the actual experimental setup such as the presence of the Germanium window. A schematic representation of the calibration setup is shown in figure 6, which

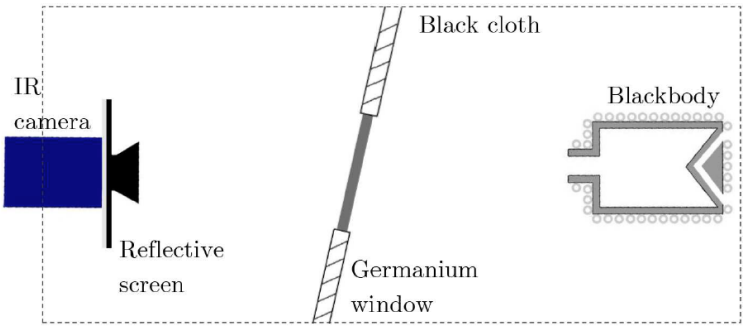

***Fig. 6**: Setup-for the calibration measurements.*

includes the IR camera, Germanium window and a thermal blackbody having an apparent emissivity of 0.999 [-] [9]. To avoid the reflection of the camera sensor from interfering with the calibration (i.e. Narcissus effect), the window is positioned under an angle (~15°) with respect to the blackbody aperture. Furthermore, the whole system is covered by a black cloth to shield it from the ambient. The blackbody is temperature controlled by heated water coming from a Tamson TLC2 thermal bath. Each point on the calibration curve is defined by simultaneously logging the temperatures of the blackbody and digital level of the blackbody aperture. The blackbody temperature is defined as the average registered by entrance and exit thermocouples, which have a maximum variation of ~0.5 *K* at 355 *K*. The *DL* is recorded as the mean of an area within the blackbody aperture (figure 7). The final representation of the calibration curve is shown in figure 8.

The surface of the test plates consists of coated copper wires, which can be approximated as a grey body emitter. The emissivity of the plate, ε_s is estimated by replacing the blackbody by a heated test plate (figure 6), and monitoring its *DL* for six surface temperatures (measured by a thermocouple) ranging from 300 – 350 *K*. In order to determine the emissivity, the recorded digital levels (E_{meas}) are compared to those observed for a black body at the same temperature (E_o), corrected for the ambient (E_{amb}):

$$\varepsilon = \frac{E_{meas} + E_{amb}}{E_o - E_{amb}} \tag{1}$$

A recorded sample image used for the emissivity computation is shown in figure 9. The mean ε_s is found to be 0.88 ± 0.02 [-], which is a reasonable variation for the assumption of the model surface as grey body.

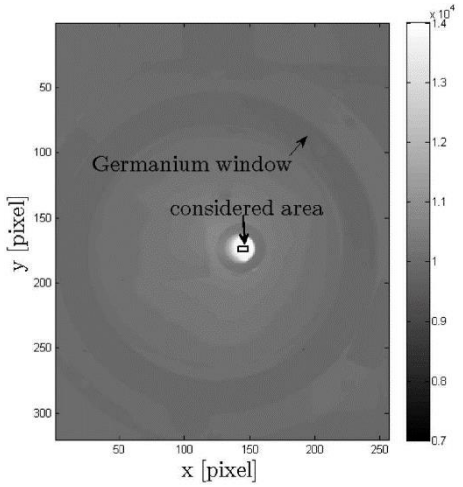

***Fig. 7**: DL recording area for calibration.*

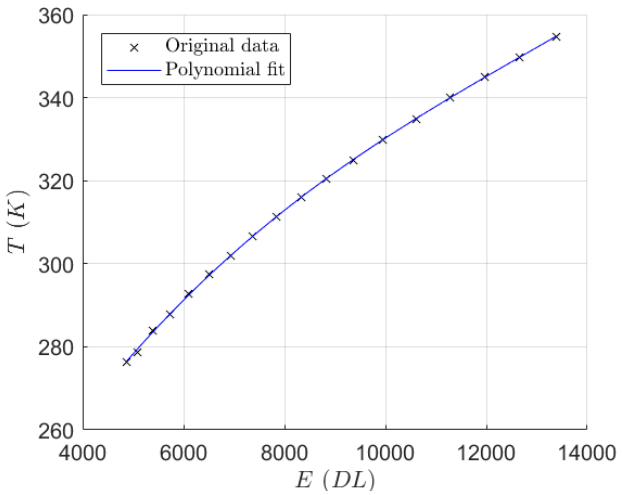

***Fig. 8**: Calibration measurements, incl. least-squares optimized polynomial curve fit.*

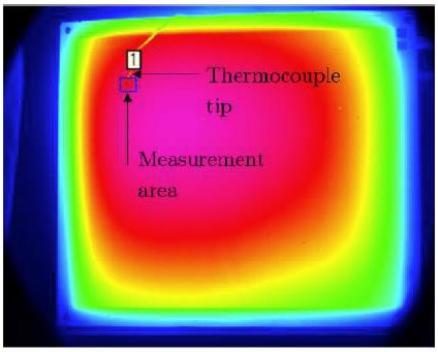

***Fig. 9**: Recorded image for test plate emissivity computation.*

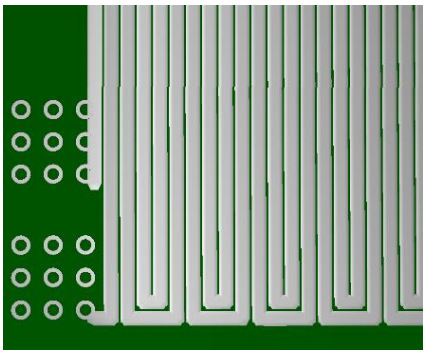

***Fig. 10**: Serpentine shaped PCB copper wire layout, incl. detailed connector pads.*

4. QIRT data reduction

The data reduction technique is based on the heat balance equation, delivering the heat transfer coefficient:

$$h = \frac{q_{conv}}{T - T_{aw}} = \frac{q_{el} - q_{cond} - q_{rad}}{T - T_{aw}}, \tag{2}$$

where q_{conv} is the convective heat transfer, while q_{el}, q_{cond}, q_{rad} are the electric heat generation, the conductive heat transfer and the radiative heat transfer, respectively. The latter three terms are each determined separately from the measurements. This approach is only valid when there is a thermal equilibrium across the surface. In the measurements this was ascertained by monitoring the temperature transient at multiple surface locations.

In turn, the Stanton number (*St*) is computed using the free stream flow conditions as the reference velocity and density:

$$St = \frac{h}{\rho_e u_e c_p}. \tag{3}$$

For each experiment, three measurements were conducted: (1) unheated, flow-off measurements, (2) heated, flow-off measurement and (3) heated, flow-on measurement. The first measurement is conducted to correct for camera and background reflections. The second measurement is used to correct for heating imperfections in the PCB. The third measurement represent the actual wind tunnel test, where the effects of the roughness geometry on the convective heat transfer are recorded. A schematic representation of the complete data reduction routine is shown in figure 11.

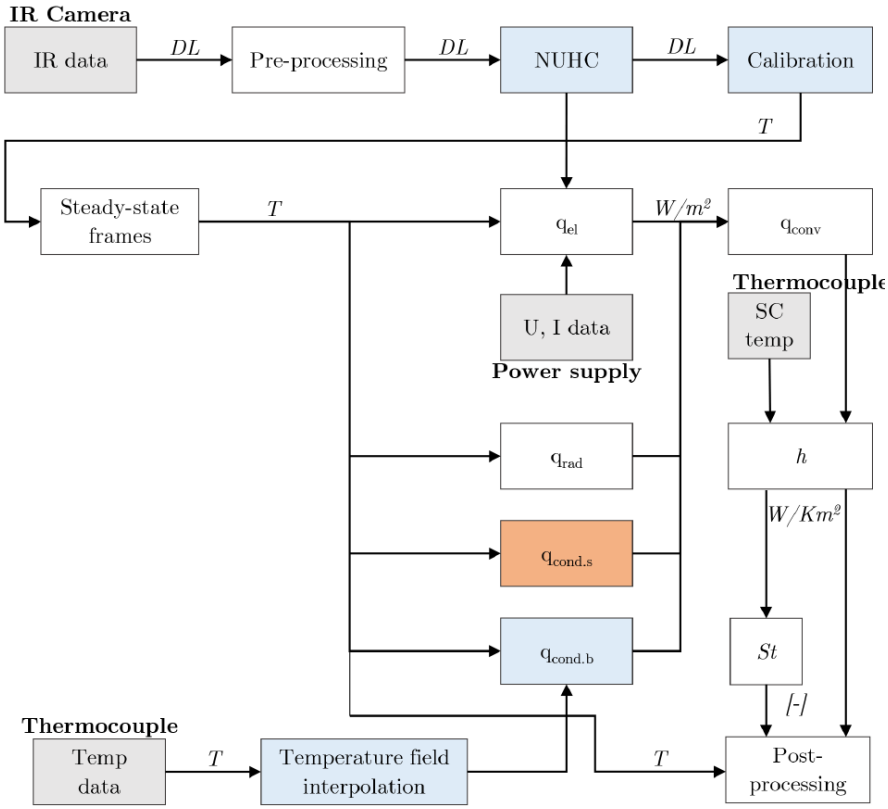

***Fig. 11**: Flowchart of QIRT data reduction routine.*

4.1. Non-uniform heating correction

In pre-processing, the unheated measurements in *DL* are subtracted from the heated, flow-off and wind tunnel measurements to eliminate camera reflections and other ambient effects. The calibration curve is adjusted accordingly. In addition to the external effects, also the non-uniform heating of the PCBs must be corrected for. By the etching process of the originally copper clad plates, minor fluctuations in thickness occur across the surface area of each PCB. As a result, a non-uniform heating and thus a non-uniform temperature distribution occurs on the PCB even whilst under natural convection. To correct for this non-uniformity, the wind tunnel models are heated without the wind tunnel running. Then, IR images are taken such to visualize and quantify their thermal signature and form a non-uniform heating correction (NUHC) matrix.

In order to determine the NUHC, a test plate is heated to a steady state under natural convection conditions (20 *W*, ~5 *min*). An order of magnitude analysis shows that for these conditions the observed non-uniformity in temperature closely corresponds to the non-uniformity in heating since heat transfer mainly happens through radiation (q_{rad} *~ 94%,* q_{conv} *~2%* and q_{cond} *~4%* [10]). So it can be stated that for a flow-off, heated measurement $q_{el} \sim q_{rad}$. Since the layout of the PCB resembles a serpentine pattern (figure 10), and the track width w_c is nearly constant (except at the turns), the local variation in resistance depends primarily on the local thickness of the tracks t_c (see discussion above) according to [11]:

$$R(i,j) = \frac{L}{\kappa w_c t_c(i,j)}, \tag{4}$$

where κ is the (temperature dependent) resistivity of copper and L is the total length of the track. Once the local variation in the resistance is determined, the heating can be obtained:

$$q_{el}(i,j) = R(i,j)I^2. \tag{5}$$

From the above, it is apparent that the local electric power input is inversely proportional to the thickness of the copper wires, i.e. $q_{el} \sim t_c^{-1}$. The NUHC is now determined as follows:

$$NUHC(i,j) = \frac{E_{avg}}{E(i,j)}, \tag{6}$$

where E_{avg} is the average radiation of the PCB surface and $E(i,j)$ corresponds to the local radiation levels in *DL*. As each PCB is unique with specific non-uniformities, each surface has an individual heating signature. Through the above described procedure, a unique NUHC is determined for each PCB. In turn, this NUHC is applied to each wind tunnel measurement for that specific plate by multiplying the NUHC with the electrical heating before inserting it into the heat balance Eq. (2).

4.2. Verification and validation

For each configuration, three wind tunnel tests are performed at different electric power inputs. At each of these power inputs, a steady thermal state was reached. By performing these measurements three times, the repeatability of the system was verified independent of power input as the same *St* values should be found. An extensive validation of the QIRT system was performed to validate the accuracy of the data obtained. Based on an order-of-magnitude analysis, the systemic error (which is mainly governed by the determination of q_{el} and q_{cond}) was estimated to be 5%. In turn, the overall data variance over the repeated experiments was 1.2%. The observed *St*-profiles clearly displayed the modified insulation/heat transfer effects associated with the flow phenomena observed from Schlieren and PIV (figure 13). An example of a quantitative comparison is shown in figure 12, where the streamwise, centerline cavity profiles of *St* and the non-dimensionalized Reynolds shear stress, $\overline{u'v'}/u_e^2$ are plotted against one another.

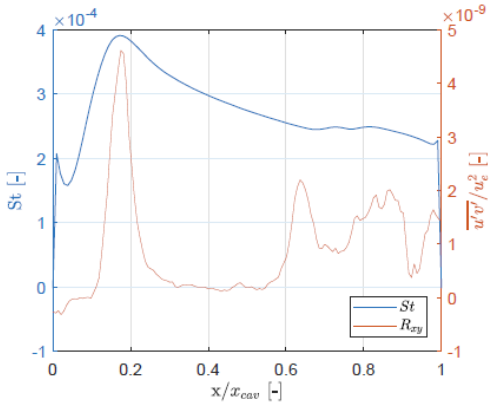

***Fig. 12**: St versus $\overline{u'v'}/u_e^2$ for 0.4/25 model.*

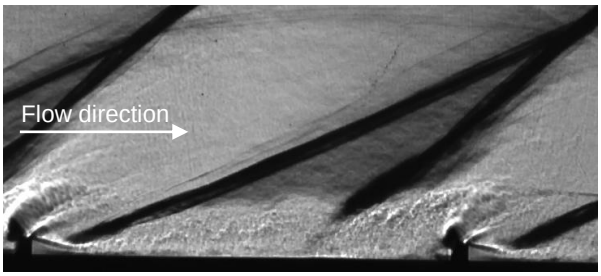

***Fig. 13**: Schlieren image for 0.4/25 model, displaying the characteristic delta wave flow discontinuity structure.*

It is chosen to compare the *St*-profiles (measured directly from the cavity surface), with the Reynolds stress of the boundary layer (measured right above the crest of the ribs), as the turbulent mixing is a good indicator for heat transfer [7]. Both profiles in figure 12 and the Schlieren image of figure 13 display the flow features for a closed cavity-type flow, namely: recirculation, reattachment, boundary layer development, flow separation, impingement and recirculation. The *St* levels have been validated quantitatively by comparing the flat plate measurements to the Reynolds analogy, respectively *St* equal to $1.9 \cdot 10^{-3}$ and $1.8 \cdot 10^{-3}$ [-].

5. Experimental results

An example of the measured convective heat transfer contour maps is shown in figures 13 and 14, corresponding to geometries of respectively *p/e* = 10 and 20 at the same relative height *e/δ* = 0.4.

***Fig. 14**: Heat transfer coefficient distribution for p/e = 10 and e/δ = 0.4.*

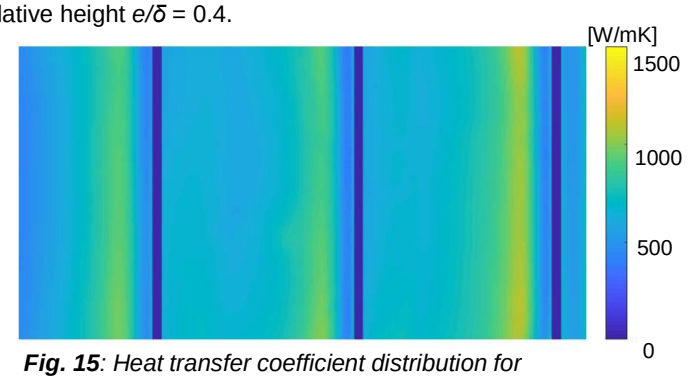

***Fig. 15**: Heat transfer coefficient distribution for p/e = 20 and e/δ = 0.4.*

From these images, it becomes evident that the change in relative pitch has a direct impact on the heat transfer distribution within the repeated cavities. However from the contour plots it is difficult to observe more subtle differences. Therefore, in order to conduct a quantitative comparison, the streamwise centerline heat transfer profiles of the last cavity of each geometry were extracted. The presentation of the experimental results is subdivided in sequences where either the relative pitch (*p/e*) or the relative height (*e/δ*) varies. This is to form a better understanding on the isolated effects of either major parameter.

5.1. The effect of relative pitch

The designed wind tunnel geometries contain a sequence of six wind tunnel models, which have an incremental change in relative pitch, *p/e* ranging from 5 to 30 at a fixed relative height, *e/δ* of 0.4. The nomenclature used to refer to these geometries is given by for example, '0.4/20', indicating a geometry with a *e/δ* of 0.4 at a *p/e* of 20 [-].

Overall, it is observed that the relative pitch has an important influence on the cavity flow topology. Similarly to what is observed for subsonic flow conditions, increasing the *p/e* initiates the transition from open-to-transitional-to-closed cavity flows [1]. This is revealed by the appearance of local heat transfer maxima (related to flow reattachment) and minima (related to recirculation and insulation). In figure 16, the heat transfer profiles are shown for relative pitches 5 up to 20, whereas figure 17 displays the profiles for *p/e* 20 up to 30.

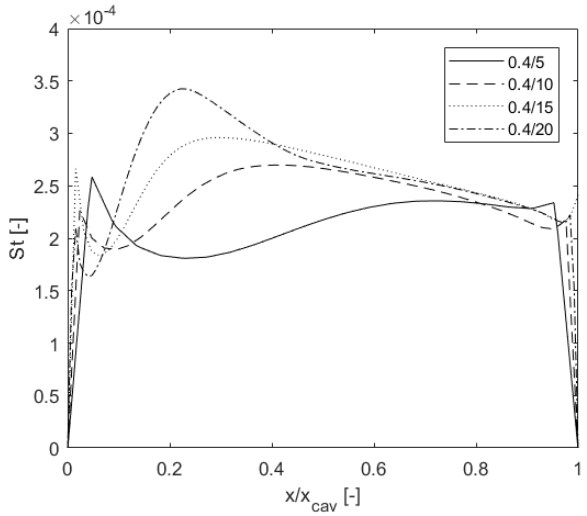

***Fig 16**: Heat transfer profiles for p/e = 5, 10, 15 and 20 at a e/δ of 0.4.*

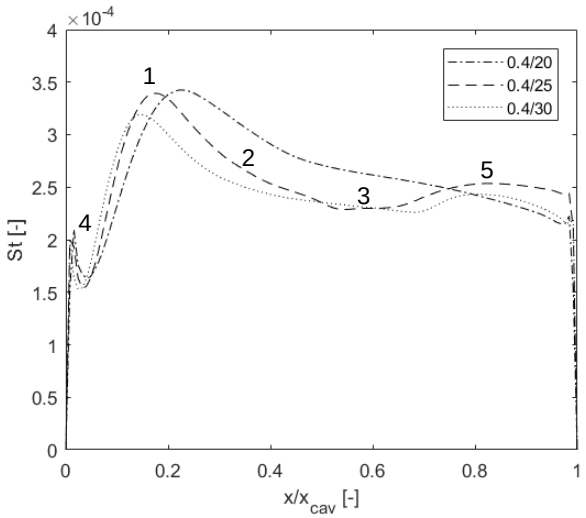

***Fig 17**: Heat transfer profiles for p/e = 20, 25 and 30 at a e/δ of 0.4.*

The transition of cavity type flow topology is illustrated in figure 16, where the first dramatic flow topological change is initiated between a *p/e* of 5 and 10, followed by the transition between *p/e* of 15 and 20. This agrees with the observations made by Stallings and Wilcox (1987) and Zhang et al. (2002), who defined the classification of supersonic cavity type flows for $p/e \leq 10$ as open, $10 < p/e < 15$ as transitional and $p/e > 15$ as closed [11,12].

At a *p/e* of 5, an open cavity profile is formed across the entire test plate geometry. As found from the Schlieren image in figure 18a, such a topology is characterized by a trapped stable vortex between the ribs. The presence of this vortex forces the boundary layer to transcend the crest of the ribs, effectively insulating the cavity floor. The *St*-profile in figure 16 indicates this insulating effect through the local minimum in heat transfer, followed by a slight increase in *St*. The subtle variation in *St* is the result of the upstream recirculation, followed by a slight growth of the shear layer combined with a thinning vortex.

For the geometries with $10 \leq p/e < 15$, the boundary layer barely impinges the cavity floor after a region of recirculation. Nevertheless, with increasing cavity length, a stronger expansion wave is formed forcing the shear layer towards the cavity floor. As such, the upstream insulating effect diminishes for increasing *p/e*. This is shown clearly in figure 16, where between the profiles of 0.4/10 and 0.4/15 a stronger heat transfer peak is formed. The near-impingement location is followed by a strong redirection of the boundary layer, which is dispersed into the freestream. As such, this deflection hinders the promotion of heat transfer.

The geometry with a *p/e* of 15 marks the transition into a closed cavity flow with the impingement of the boundary layer on the cavity floor [13]. Yet, the cavity profile of 0.4/15 does not indicate all the attributes typical to closed cavity flow. These attributes are observed as a rapid increment in *St*, followed by a subtle and sharp decrement, caused by respectively boundary layer reattachment, development and flow separation. At the transition of these events, flow discontinuities occur (impingement and exit shock), forming a delta wave structure. The observations made with regards to heat transfer are in-line with the corresponding Schlieren image, which shows that the required delta wave structure only emerges for the first cavity of the 0.4/15 geometry and disappears for the subsequent cavities (figure 18.b).

The prolonged presence of the delta wave structure, typical to a closed cavity flow, is visible for all geometries for which $p/e > 15$ (figure 18c). From figure 17, it is found that reattachment strongly increases the *St* (1), whereas the growing

boundary layer insulates the floor (2); reducing the level of heat transfer. Finally, a decline in *St* aims at the flow separation location (3), equivalent to the origin of the downstream oblique shock wave. The delta wave structures are surrounded by an upstream and downstream recirculation region (4, 5) which both reduce the local heat transfer. The first does this by the formation of a stable vortex region before the impingement shock, whereas the latter forms a stable vortex behind the exit shock due to interaction of the stagnated flow with the separated boundary layer.

In figure 16, the transition from transitional to closed cavity flow is depicted by the steep increment in upstream heat transfer (corresponding to flow reattachment). In turn, the profiles in figure 17 effectively display the same flow features, where with the increase of pitch the boundary layer development embodies a growing portion of the complete cavity length; increasing the overall heat transfer. However, between the models with *p/e* 25 and 30, a decline exists between the heat transfer peak and the overall *St* levels. By the Schlieren images, this was found not to be caused by a weaker boundary layer interaction. Rather, PIV data suggests that this decline in *St* is directly related to lower turbulence levels for the 0.4/30 model.

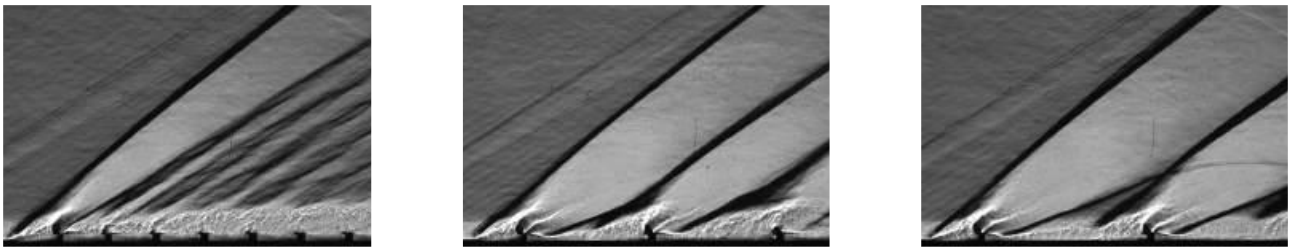

a. ***b.*** ***c.***

Fig 18*: Schlieren images for 0.4/5 (a), 0.4/15 (b) and 0.4/20 (c).*

5.2. The effect of relative height

The previous discussion has indicated that flow phenomena characteristic to specific cavity type flows are reflected in the heat transfer profiles. The respective appearance of these flow phenomena is determined by the value of *p/e*. It is expected that each cavity type flow reacts differently to changes in relative rib height, *e/δ*. Therefore, the effect of *e/δ* is investigated by displaying the *St* cavity profiles for respectively *open*, *transitional* and *closed* type flows. In general, two primary effects can be distinguished by the increase of *e/δ,* namely (1) invariance in cavity flow topology, and (2) an overall decrease in heat transfer. The reasons behind the cavity-average decrease in heat transfer, however, are different for each cavity type flow.

In the case of open cavity flow, spark-Schlieren images suggest that the boundary layer freely passes over the crest of the ribs. This effect is seen to hold for all rib heights tested (compare figures 18a and 21a). As such, any increment in rib height increases the distance between the boundary layer and cavity floor; strengthening the stable recirculation region within the cavities. This insulating effect is illustrated in figure 19, where between 0.4/5 and 0.8/5 the upstream *St* levels are found to decrease. The fact that case 0.2/5 differs considerably from the rest can be explained by the limited

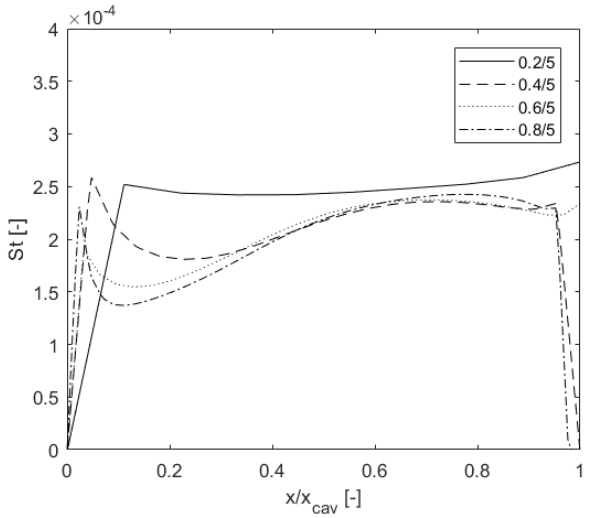

Fig 19*: Heat transfer profiles for p/e = 5 at a e/δ of 0.2, 0.4, 0.6 and 0.8 [-].*

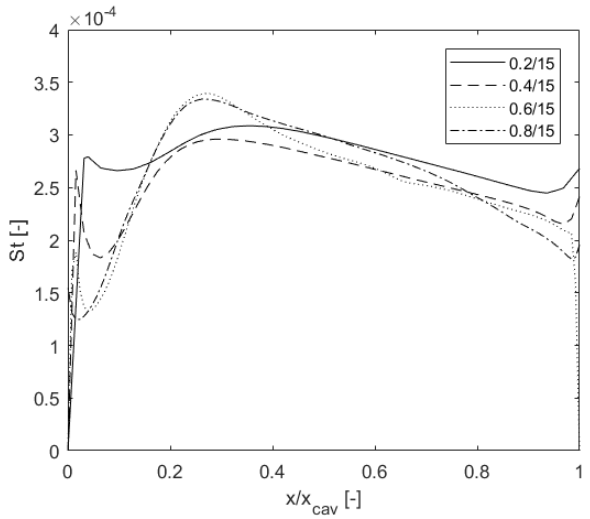

Fig 20*: Heat transfer profiles for p/e = 15 at a e/δ of 0.2, 0.4, 0.6 and 0.8 [-].*

resolution of the depicted cavity. As the system resolution is limited to 1.6 pixels/*mm* and the cavity size is 6 *mm*, approximately four data points are present for this geometry measurement. Therefore, this profile is not further studied in detail in this analysis and only shown for completeness.

The heat transfer profiles for the transitional cavity flows (figure 20) display that the increments in *e/δ* enhance the insulation effects of the upstream recirculation region. This is likely to be caused by the occurrence of stronger shock waves for each model (figure 21b). Furthermore, the flow phenomena specific to transitional cavity type profiles remain identifiable. The heat transfer peaks of boundary layer reattachment, as well as the decrease in heat transfer due to boundary layer development are seen to decrease from 0.2/15 to 0.4/15, followed by an increment at 0.6/15 to 0.8/15. Still, the differences in overall *St* levels between models at 0.6 and 0.8 are small relative to the smaller versions. This is likely to be caused by the indifference in the number of ribs the flow has gone over prior to monitoring the final cavity. Whereas there exists a difference of four rib passes between the 0.2/15 and 0.4/15 geometries, both 0.6/15 and 0.8/15 hold two ribs upstream the final cavity. The results suggest that the number of rib passes has a more dominant effect on the heat transfer, than the size of the ribs themselves. Through each rib collision, more momentum is lost by the boundary layer and the turbulence levels are enhanced (as supported by analogous PIV data). As a result of this repetitive process, the boundary layer becomes developed leading to a more transitional-type cavity flow. This could be the reason for the more flattened *St* profiles, found for the smaller geometries.

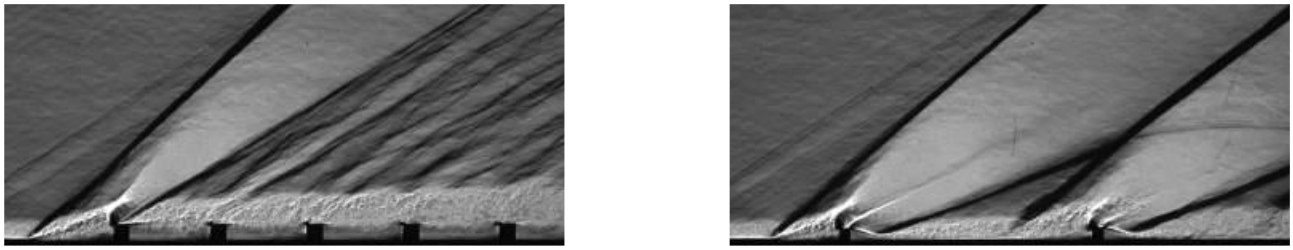

a. ***b.***

Fig 21*: Schlieren images for 0.6/5 (a) and 0.6/20 (b).*

The geometries resulting in a closed cavity type flow depict effects similar to the transitional cavity flow case. This is observed from the *St*-profiles in figure 22, where an increase of *e/δ* strongly reduces the heat transfer directly adjacent to the upstream rib (i.e. enhancing recirculation). Apart from the effect of an exit shock wave, each profile for geometries 0.2/20, 0.4/20 and 0.6/20 indicates all features belonging to the typical delta wave structure (figure 13). The effect of the exit shock is most optimally observed in the 0.6/20 trend line. Directly after the near-linear *St* decrease (i.e. boundary layer development), a peak in heat transfer occurs. The nick between these flow phenomena corresponds to the location of the exit shock wave. The slight peak following the exit is the result of turbulated flow, which develops by interacting with decelerated flow downstream the cavity.

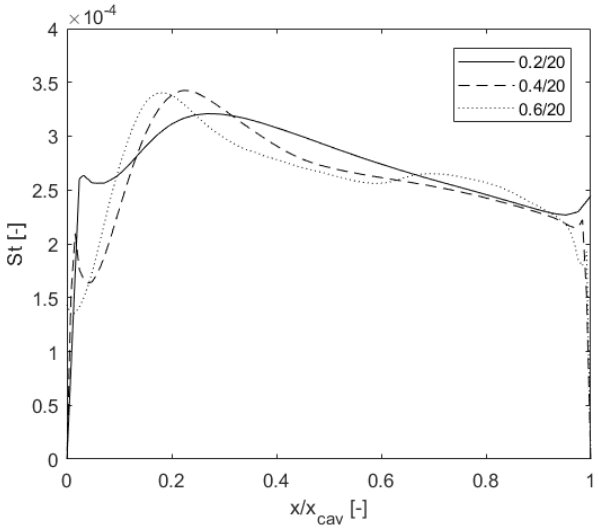

Fig 22*: Heat transfer profiles for p/e = 20 at a e/δ of 0.2, 0.4, and 0.6 [-].*

6. Conclusion

The present experimental study provides quantitative insight on the influence of large ($e/\delta \geq 0.2$), ribbed wall roughness elements on the heat transfer of a turbulent, supersonic boundary layer that complements the existing data base on the heat transfer characteristics and associated flow topologies of these geometries. Quantitative infrared thermography (QIRT) was selected as primary diagnostic technique to provide the desired data. An experimental setup was designed and built tailored to the used wind tunnel. Through the defined experimental approach, involving three types of wind tunnel measurements, and the associated data reduction technique, the method was found to be highly repeatable as overall variance remained below 1.2%. A comparison of flat plate measurements with theory displayed a deficiency of approximately 5%. As such, the QIRT technique proved both accurate and reliable.

The wind tunnel experiments on the different rough plate geometries have provided the following conclusions with respect to the cavity flow characteristics and corresponding heat transfer profiles. At $p/e < 10$, an open cavity flow profile is formed across the rib pairs over the entire length of the test plates. For such cavity flow fields, a stable recirculating flow prevents the turbulent boundary layer from directly interacting with the cavity floor. From the *St*-profile, it is seen that after the upstream recirculation more heat transfer takes place. This is in line with the growing shear layer thickness as identified in Schlieren images. Around p/e = 10, evidence of a transitional cavity profile is given and is recognized by a stronger upstream insulation region followed by an increase in *St*. These phenomena correlate with a shear layer impingement on the cavity floor, followed by a strong flow deflection. For all configurations where $p/e > 15$, closed-cavity profiles are found. In these *St*-profiles, a strong insulation region (recirculation), followed by a steep increase (corresponding to flow reattachment on the cavity floor), a linear decline (boundary layer growth) and short increment (rib collision) are found. The *St*-profiles have thus revealed that the relative pitch ratio, p/e greatly influences the flow topologies of the turbulent boundary layer. This observation is supported by the Schlieren and PIV data. The effect of relative roughness height, e/δ, however, was found to be insignificant on the flow topology whilst decreasing overall *St* levels. For open cavity flows, this is caused by an increased distance between the turbulent boundary layer and the cavity floor. In the case of closed cavity flows, the reduced number of rib collisions is detrimental to the enhancement of turbulence and thus heat transfer. By combining these findings with respect to the isolated effects of respectively p/e and e/δ, it is estimated that largest average *St* is found for the geometry with a e/δ of 0.2, and a p/e of 25.

REFERENCES

[1] D. A. Aliaga, D. E. Klein, and J. P. Lamb, “Heat Transfer Measurements on a Ribbed Surface At Constant Heat Flux Using Infrared Thermography”, Experimental Heat Transfer, vol. 6, no. 1, pp. 17–34, 1993.
[2] J. C. Han, “Heat Transfer and Friction in Channels With Two Opposite Rib-Roughened Walls”, Journal of Heat Transfer, vol. 106, no. 4, p. 774, 1984.
[3] J. C. Han, J. S. Park, and C. K. Lei, “Heat Transfer Enhancement in Channels With Turbulence Promoters.”, Journal of Engineering for Gas Turbines and Power, vol. 107, no. 3, pp. 628–635, 1985.
[4] B. Hodge and R. Taylor, “Application of the Discrete-Element Surface Roughness, Model to Rocket Nozzle Heat Transfer Computation”, AIAA-91-2435, vol. 27, 1991.
[5] J. Jimenez, “Turbulent Flows Over Rough Walls”, Annual Review of Fluid Mechanics, vol. 36, no. 1, 2004.
[6] R. M. Latin and R. D. W. Bowersox, “Flow Properties of a Supersonic Turbulent Boundary Layer with Wall Roughness Introduction”, AIAA journal, vol. 38, no. 10, pp. 1804–1821, 2000.
[7] T. M. Liou and J. J. Hwang, “Turbulent Heat Transfer Augmentation and Friction in Periodic Fully Developed Channel Flows”, Journal of Heat Transfer, ASME, vol. 114, no. February 1992, pp. 56–64, 1992.
[8] Z. Sun, F. F. J. Schrijer, F. Scarano, and B.W. van Oudheusden, “The three-dimensional flow organization past a micro-ramp in a supersonic boundary layer”, Physics of Fluids, vol. 24, no. 5, pp. 1–22, 2012.
[9] R. Mayer, “Orientation on quantitative ir-thermography in wall-shear stress measurements”, Delft University of Technology, Faculty of Aerospace Engineering, Report LR-812, 1996.
[10] F. Kreith, R. M. Manglik, and M. S. Bohn, Principles of heat transfer. Cengage learning, 2012.
[11] T. Astarita and G. M. Carlomagno, Infrared thermography for thermo-fluid-dynamics. Springer Science & Business Media, 2012.
[12] J. Zhang, E. Morishita, T. Okunuki, and H. Itoh, “Experimental investigation on the mechanism of flow-type changes in supersonic cavity flows”, Transactions of the Japan.
Society for Aeronautical and Space Sciences, vol. 45, no. 149, pp. 170–179, 2002.
[13] R. L. Stallings Jr. and F. J. Wilcox Jr., “Experimental cavity pressure distributions at supersonic speeds”, 1987.